J. Fluid Mech. (1995), *vol.* 305, *pp.* 159–183

A numerical study of turbulent supersonic isothermal-wall channel flow

By G. N. COLEMAN[1], J. KIM[1] AND R. D. MOSER[2]†

[1] Mechanical, Aerospace, and Nuclear Engineering Department, UCLA, 48-121 Engr. IV, Box 951597, Los Angeles, CA 90095-1597, USA

[2] NASA Ames Research Center, Moffett Field, CA 94035-1000, USA

(Received 31 December 1994 and in revised form 11 May 1995)

A study of compressible supersonic turbulent flow in a plane channel with isothermal walls has been performed using direct numerical simulation. Mach numbers, based on the bulk velocity and sound speed at the walls, of 1.5 and 3 are considered; Reynolds numbers, defined in terms of the centreline velocity and channel half-width, are of the order of 3000. Because of the relatively low Reynolds number, all of the relevant scales of motion can be captured, and no subgrid-scale or turbulence model is needed. The isothermal boundary conditions give rise to a flow that is strongly influenced by wall-normal gradients of mean density and temperature. These gradients are found to cause an enhanced streamwise coherence of the near-wall streaks, but not to seriously invalidate Morkovin's hypothesis: the magnitude of fluctuations of total temperature and especially pressure are much less than their mean values, and consequently the dominant compressibility effect is that due to mean property variations. The Van Driest transformation is found to be very successful at both Mach numbers, and when properly scaled, statistics are found to agree well with data from incompressible channel flow results.

1. Introduction

This paper addresses the effects of compressibility on supersonic wall-bounded turbulence. These can be broadly categorized as one of two types: those associated with variations of the mean properties (such as density and viscosity), and those due to fluctuations of thermodynamic quantities. It is often assumed that only the mean effects are significant for transonic and supersonic wall-bounded flows (those with free-stream Mach number less than about 5) (Bradshaw 1977; Spina, Smits & Robinson 1994). A main objective of the present work is to quantify the degree to which this is in fact true. Another is to evaluate modelling concepts such as the Morkovin hypothesis and the Van Driest transformation (Bradshaw 1977).

To this end we have undertaken a direct numerical simulation (DNS) study of turbulent supersonic flow in an isothermal-wall plane channel. Mach numbers, based on wall temperature and bulk velocity, of 1.5 and 3 are utilized. Because all relevant temporal and spatial scales of motion are resolved, no subgrid-scale or turbulence model is needed; however, finite computer resources limit the simulations to relatively

† Present address: Department of Theoretical and Applied Mechanics, University of Illinois, Urbana, IL 61801 USA.

low Reynolds numbers (values of the order of 3000, based on mean centreline velocity and channel half-width).

The first compressible DNS studies were of flows in open domains. (For an overview of the experimental and theoretical compressible turbulence work done to date readers are referred to review articles by Bradshaw (1977), Lele (1994) and Spina *et al.* (1994); catalogues of compressible boundary layer experimental data have been developed by Fernholz & Finley (1977, 1980), Fernholz *et al.* (1989) and Settles & Dodson (1991).) These open-domain DNS studies, which are reviewed in Lele (1994), provide a useful reference in our attempt to isolate compressibility effects unique to wall-bounded flows. Of even more relevance here are the recent supersonic boundary layer DNS of Guo & Adams (1994) and Rai, Gatski & Erlebacher (1995). Because both groups impose adiabatic boundary conditions and consider the spatially developing layer, their mean profiles will differ from those presented below. Thus, a direct comparison of the Guo & Adams and Rai *et al.* data with the present date is not possible. An adiabatic wall is also used by Ducros, Compte & Lesieur (1993), Guo, Kleiser & Adams (1994) and Hatay & Biringen (1995). Ducros *et al.* and Guo *et al.* use DNS to investigate transition of temporally and (by the latter) spatially evolving Mach 4.5 layers; the former also use large-eddy simulations to compute the resulting high-Reynolds-number fully turbulent flow. Hatay & Biringen perform DNS of a steady parallel-flow Mach 2.5 boundary layer. In the future it is expected that these complementary studies (see also Childs & Reisenthel 1995) will illuminate behaviour that is common to all wall-bounded compressible turbulence.

For the Mach number range investigated in this study we find that most quantities of engineering interest are dominated by variable-property effects, and both the Morkovin hypothesis and the Van Driest transformation are on the whole quite successful. However, 'pure compressibility' effects are not totally negligible. For example, significant large-scale acoustic fluctuations are found between the channel walls, although they do not strongly alter the vortical field (cf. Kovásznay 1953). A noteworthy 'structural' change is observed, however, in that the near-wall streaks become more coherent in the streamwise direction as the Mach number increases. The evidence for and explanation of these phenomena will be presented below. We will also discuss the accuracy and limitations of the numerical results, compare the data to those found for the incompressible channel, illustrate the invariance to (supersonic) Mach number of properly scaled statistics, and address the basic modelling issues mentioned above; further analysis of the modelling implications of the DNS results (such as the relative merits of Favre and ensemble averaging) is given in Huang, Coleman & Bradshaw (1995), which can be viewed as a companion to this paper.

2. Problem formulation and numerical approach

The plane channel geometry was chosen so that finite Mach number effects can be isolated by comparing the present results to well-established incompressible channel data (Kim, Moin & Moser 1987). Here the fluid is assumed to be an ideal gas with constant specific heats, constant Prandtl number, and power-law temperature-dependent viscosity. Isothermal-wall boundary conditions are imposed so that a statistically stationary state can be obtained. The flow is driven by a uniform (in space) body force (rather than a mean pressure gradient) to preserve streamwise homogeneity, with the body force chosen to vary in time such that the total mass flux remains constant.

In what follows, all quantities are non-dimensionalized by the wall temperature, the

channel half-width, the bulk-averaged ('mixed-mean') density, and the bulk velocity, such that $\frac{1}{2}\int_{-1}^{+1}\langle\rho\rangle \mathrm{d}y = 1$ and $\frac{1}{2}\int_{-1}^{+1}\langle\rho u\rangle \mathrm{d}y = 1$, where the channel walls are at $y = \pm 1$. We use ρ to represent the density, $u = u_1$ the streamwise velocity, $(x, y, z) = (x_1, x_2, x_3)$ respectively the streamwise, wall-normal, and spanwise coordinates, and angle brackets denote an average over time and streamwise and spanwise directions. The non-dimensional governing equations are then

$$\frac{\partial \rho}{\partial t} + u_j \frac{\partial \rho}{\partial x_j} = -\rho \frac{\partial u_j}{\partial x_j}, \tag{1}$$

$$\frac{\partial u_i}{\partial t} + u_j \frac{\partial u_i}{\partial x_j} = -\frac{1}{\gamma M^2}\frac{\partial T}{\partial x_i} - \frac{T}{\gamma M^2 \rho}\frac{\partial \rho}{\partial x_i} + \frac{1}{Re\,\rho}\frac{\partial \tau_{ij}}{\partial x_j} + \Phi_i, \tag{2}$$

$$\frac{\partial T}{\partial t} + u_j \frac{\partial T}{\partial x_j} = -(\gamma - 1)T\frac{\partial u_j}{\partial x_j} + \frac{\gamma(\gamma-1)M^2}{Re}\frac{\tau_{ij}}{\rho}\frac{\partial u_i}{\partial x_j} - \frac{\gamma}{Re\,Pr\,\rho}\frac{\partial Q_j}{\partial x_j} + \mathscr{S}, \tag{3}$$

where

$$\tau_{ij} = \mu\left(\frac{\partial u_i}{\partial x_j} + \frac{\partial u_j}{\partial x_i} - \frac{2}{3}\delta_{ij}\frac{\partial u_l}{\partial x_l}\right) \quad \text{and} \quad Q_j = -\mu\frac{\partial T}{\partial x_j}.$$

Since the pressure is normalized by the bulk density and bulk velocity, the ideal gas law is $p = \rho T/\gamma M^2$. The body force term Φ_i is non-zero only for $i = 1$. Furthermore, note that Φ_i, which is uniform in space, is analogous to $(-1/\rho)\partial P/\partial x$ in pressure-driven flows, so the 'equivalent pressure gradient' in (2) is *not* uniform in y (see figure 10 of Huang *et al.* 1995). (In retrospect, dividing the body force in (2) by ρ would have made the connection with pressure-driven flows more straightforward, although all qualitative and order-of-magnitude conclusions, and indeed many dimensionless parameters such as spectrum shapes and correlation coefficients, obtained here will also apply to the pressure-driven case.) The purpose of $\mathscr{S}$, the source/sink term in (3), is explained below. Equations (1)–(3) are solved numerically subject to the isothermal, no-slip boundary conditions,

$$T = 1 \quad \text{and} \quad \boldsymbol{u} = 0 \quad \text{at} \quad y = \pm 1. \tag{4}$$

No boundary conditions on density or pressure are imposed; instead the integral constraint that the bulk density remain constant in time is applied.

Relevant non-dimensional parameters are (i) a Mach number, M, based on the bulk velocity and wall sound speed; (ii) a Reynolds number, Re, based on the bulk density, bulk velocity, channel half-width, and wall viscosity; (iii) the Prandtl number, Pr; (iv) the ratio of specific heats, γ; and (v) the viscosity exponent, n, where the dynamic viscosity $\mu \propto T^n$. These five parameters are used to define the various DNS runs.

Besides choosing appropriate values for the 'physical' parameters, we will also artificially introduce another to allow us to differentiate between mean and fluctuation compressibility effects. The Mach number appears in the internal energy equation (3) in the term that represents the irreversible loss of kinetic energy into heat. Following Buell (1991), we interpret (in our simulations) the actual Mach number M in (2) and the 'dissipation Mach number' (i.e. the Mach number parameter appearing in (3), denoted M_d) as separate parameters. By setting M_d to values different from M in the DNS, we produce the effective heat source/sink $\mathscr{S}$ in (3), which is given by

$$\mathscr{S} = \left(M_d^2 - M^2\right)\frac{\gamma(\gamma-1)}{Re}\frac{\tau_{ij}}{\rho}\frac{\partial u_i}{\partial x_j}. \tag{5}$$

Case	M	M_d	Re	Pr	γ	μ
A	1.5	1.5	3000	0.7	1.4	$T^{0.7}$
B	3	3	4880	0.7	1.4	$T^{0.7}$
AX	1.5	0	3000	0.7	1.4	$T^{0.7}$

TABLE 1. DNS physical parameters.

m_x	m_y	m_z	n_x	n_y	n_z	L_x	L_z
110	90	60	144	119	80	4π	$4\pi/3$

TABLE 2. DNS numerical parameters.

Consequently, we can consider cases with different mean temperature profiles (and thus different mean property variations) at the same M. Results from these 'unphysical' $M \neq M_d$ DNS runs can, therefore, be used to determine the relative importance of turbulent-fluctuation and variable-property influences at a given Mach number.

Three DNS cases will be discussed, with Mach numbers of $M = 1.5$ and 3. All the runs share the same Prandtl number, specific heat ratio, and viscosity exponent ($Pr = 0.7$, $\gamma = 1.4$ and $n = 0.7$), while the Reynolds number (for reasons given below) is either 3000 or 4880. A summary of the parameters is listed in table 1. Cases denoted by a single letter (A and B) in table 1 represent 'physical' simulations for which $M_d = M$. For the $M_d \neq M$ run, Case AX, $M = 1.5$ and $M_d = 0$. Since the temperature fields in both the physical and unphysical runs depend almost exclusively on M_d (Coleman *et al.* 1993), this parameter combination will produce the behaviour of the 'extra' source/sink $\mathscr{S}$, equation (5), that is necessary to isolate variable-property and fluctuation effects. (Note that while the body force Φ_i contributes to the kinetic energy budget, it does not appear in the internal energy equation.) With $M_d = 0$, $\mathscr{S}$ is such that the temperature and density are very nearly constant across the channel, as we shall see below.

The DNS results are generated using the code developed by Buell to study compressible Couette flow. During the computations, the body force Φ_i is adjusted so that the total mass flux through the channel remains constant, and in this sense is analogous to the mean pressure gradient in Kim *et al.*'s incompressible channel flow; once the flow reaches a statistically stationary state the variations of Φ_i with time are small. The code utilizes a Fourier–Legendre spectral discretization along with a hybrid implicit–explicit third-order four-substep time-advance algorithm designed to maximize the range of Mach numbers that can be considered (Buell 1991). The time advancement is applied to the expansion coefficients (i.e. done in 'wave space'). A 'Legendre transform' (Buell 1991), and the 'prime factor algorithm' fast Fourier transform (Temperton 1985) are used in the inhomogeneous y- and homogeneous x- and z-directions, respectively. The numerical parameters used by all three runs are given in table 2, where L_x and L_z are the streamwise and spanwise domain sizes, and (m_x, m_y, m_z) and (n_x, n_y, n_z) are respectively the number of expansion coefficients and collocation (quadrature) points in the streamwise, wall-normal, and spanwise directions. The x and z grid spacing in viscous wall units is $\Delta x^+ \approx 19$ and $\Delta z^+ \approx 12$ for Case A, $\Delta x^+ \approx 39$ and $\Delta z^+ \approx 24$ for Case B and $\Delta x^+ \approx 17$ and $\Delta z^+ \approx 10$ for Case AX; in the wall-normal direction, the first collocation point off the wall is at $y^+ \approx 0.1$, 0.2 and 0.1 – and the first ten points are within approximately $y^+ = 8$, 17 and 7 – for Cases A, B and AX, respectively. That some of these values are larger than their

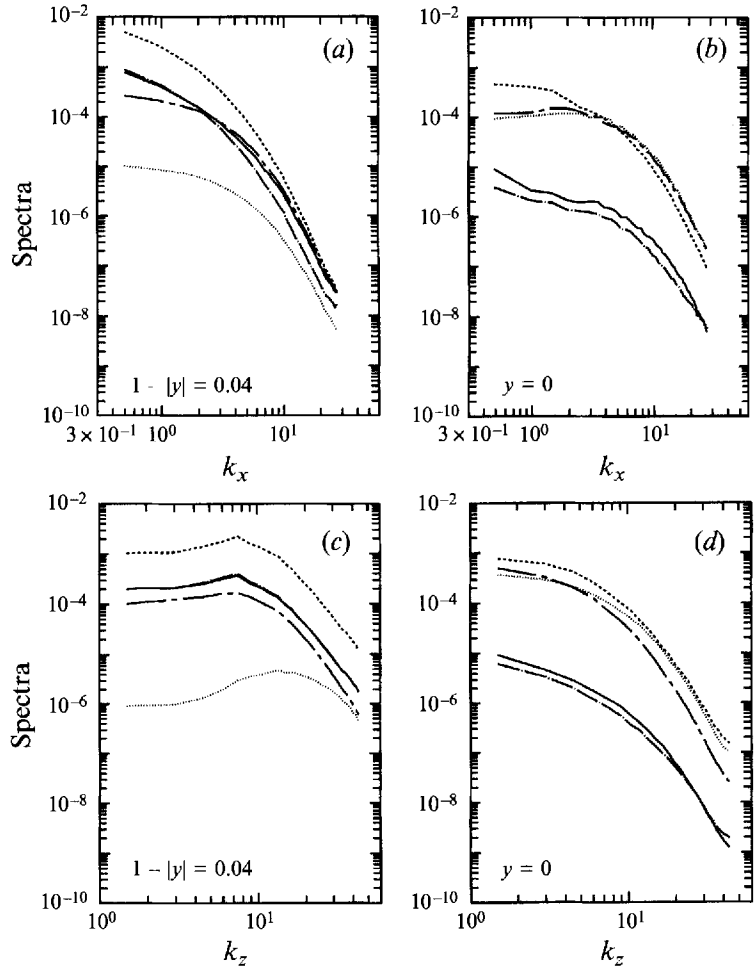

FIGURE 1. One-dimensional Fourier spectra for Case A ($M = 1.5$) at (a, c) near the wall, $1-|y| = 0.04$, and (b, d) at the centreline: ——, ρ; - - - -, u; · · · · ·, v; — - —, w; —·—, T. (a, b) Streamwise; (c, d) spanwise.

normally accepted full-resolution maxima (Kim *et al.* 1987; Spalart 1988) does not imply the present DNS are under-resolved: because of the rapid near-wall variations of mean properties, measuring the grid spacing in terms of the friction velocity and viscosity at the wall does not yield a straightforward indication of resolution quality for this flow (cf. figure 2*b* of Huang *et al.* 1995). We instead rely on energy spectra to verify that the parameters listed in table 2 are adequate (see figures 1 and 2).

Initial conditions for Case A were given by superimposing random velocity fluctuations upon a laminar parabolic velocity profile ($\langle u\rangle = 1.5(1-y^2)$, $\langle v\rangle = \langle w\rangle = 0$) and uniform density and temperature fields ($\langle\rho\rangle = \langle T\rangle = 1$); Cases B and AX used a mature Case A field. After an initial transient (during which the solutions were transferred from relatively coarse to finer grids), all three cases relaxed to a fully resolved statistically stationary state. The runs were made on the ACF and NAS Cray YMP and C-90 computers at NASA Ames Research Center. The code performed at approximately 350 Mflops on the C-90 and required about 32 CPU seconds per full timestep (four substeps). For Case B about 30 full steps are needed to advance one non-dimensional time unit.

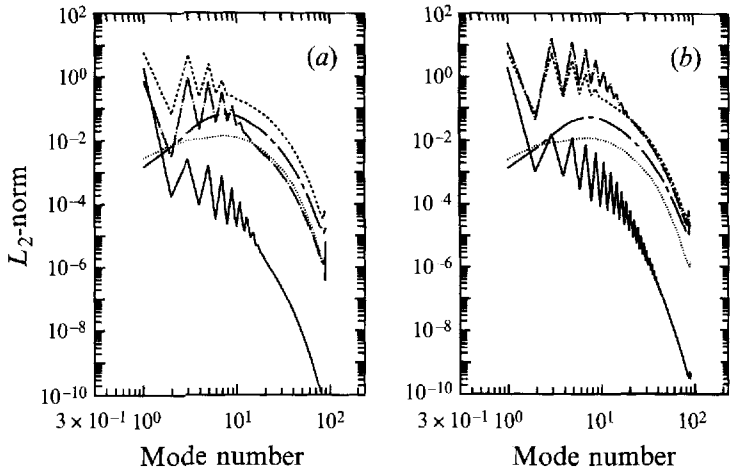

FIGURE 2. Legendre coefficient spectra (summed over k_x and k_z) for (*a*) Case A ($M = 1.5$), and (*b*) Case B ($M = 3$): symbols as figure 1. Because of orthogonality of Legendre polynomials, and the form of basis functions (Buell 1991), spectra denote the L_2-norm (Fletcher 1984) of ρ and the L_2-norm of y-derivatives of u, v, w and T.

3. Results

3.1. *'Physical' simulations* ($\mathscr{S} = 0$)

We begin by presenting data from the runs without the source/sink term, i.e. with $M_d = M$. These $M = 1.5$ and $M = 3$ results will be compared to data from Kim *et al.*'s (1987) $M = 0$ incompressible channel DNS, which will reveal the influence of increasing the Mach number into the supersonic regime. All of the statistics in this section were obtained by averaging over at least 25 fields spanning 150 non-dimensional time units.

3.1.1. *Spectra and correlations*

An indication of the numerical fidelity of the DNS is provided by the streamwise and spanwise one-dimensional spectra from the channel centreline and near the walls, shown in figure 1 for Case A. They are typical of those found from all three DNS runs – Cases A, B and AX – in their rapid fall-off at high wavenumber, which suggests that the x- and z-resolution is adequate. The high-wavenumber streamwise and spanwise spectra of the velocity at both the channel centreline (figure 1*b*, *d*) and near the wall (figure 1*a*, *c*) are similar to those found in the incompressible channel (see figure 3 of Kim *et al.* 1987). In the present simulations, we find that the density and temperature spectra are closely related to each other (which implies that $p' \ll \langle p \rangle$) and that their magnitudes are much larger near the walls than they are at the centreline. The 'Legendre spectra' for Cases A and B (figure 2) verify that the wall-normal resolution is also sufficient. The 'saw-tooth' pattern in the low-mode spectra for ρ, u and T is the result of representing functions that have symmetric means in y with orthogonal polynomials whose even and odd members are decoupled (Buell 1991).

The streamwise and spanwise correlations in figures 3 and 4 are also roughly equivalent to the incompressible results (cf. figure 2 of Kim *et al.* 1987) except for two characteristics: the large spanwise coherence of the density and temperature at the centreline (figures 3*d* and 4*d*; note the large values at $L_z/2$) and the greater streamwise coherence of the ρ, u, and T fields near the wall (figures 3*a* and 4*a*).

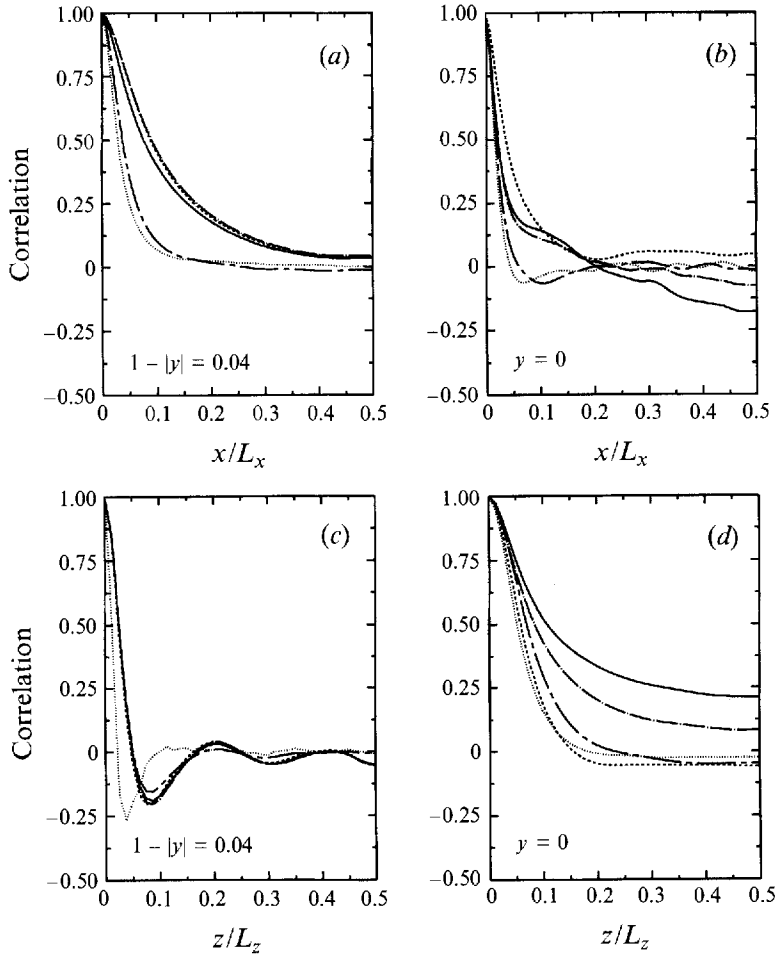

FIGURE 3. Two-point correlations for Case A ($M = 1.5$) at (a, c) near the wall, $1 - |y| = 0.04$, and (b, d) at the centreline: symbols as figure 1. (a, b) Streamwise; (c, d) spanwise.

First consider the spanwise coherence in ρ and T at the centreline, which we believe to be caused by acoustic resonance – or in other words, associated with the so-called 'acoustic mode' of compressible turbulence (Kovásznay 1953).† Evidence for this is provided by comparing the full correlations to those obtained by eliminating the contribution from several 'acoustic eigenfunctions.' This 'acoustic extraction' is done by projecting the DNS fields onto eigenfunctions of the linear inviscid isentropic problem for a base flow given by the mean density, temperature and streamwise velocity found in the DNS (see the Appendix for details). The dashed curve in figure 5 represents the density correlation obtained after the first three relevant (see the Appendix) wall-normal acoustic modes at the first three lowest-order streamwise wavenumbers k_x for $k_z = 0$ have been projected and removed from six DNS fields.

† Since entropy fluctuations are greatest near the walls (see figure 14 below) and because the mean shear couples the vorticity and dilatation perturbations – even for the linear inviscid case (Blaisdell, Mansour & Reynolds 1993) – the decomposition into 'vortical', 'entropy' and 'acoustic' modes (Kovásznay 1953) is apt to be most relevant near the centreline, where $\mathrm{d}\langle u\rangle/\mathrm{d}y$ and fluctuations of vorticity are smallest.

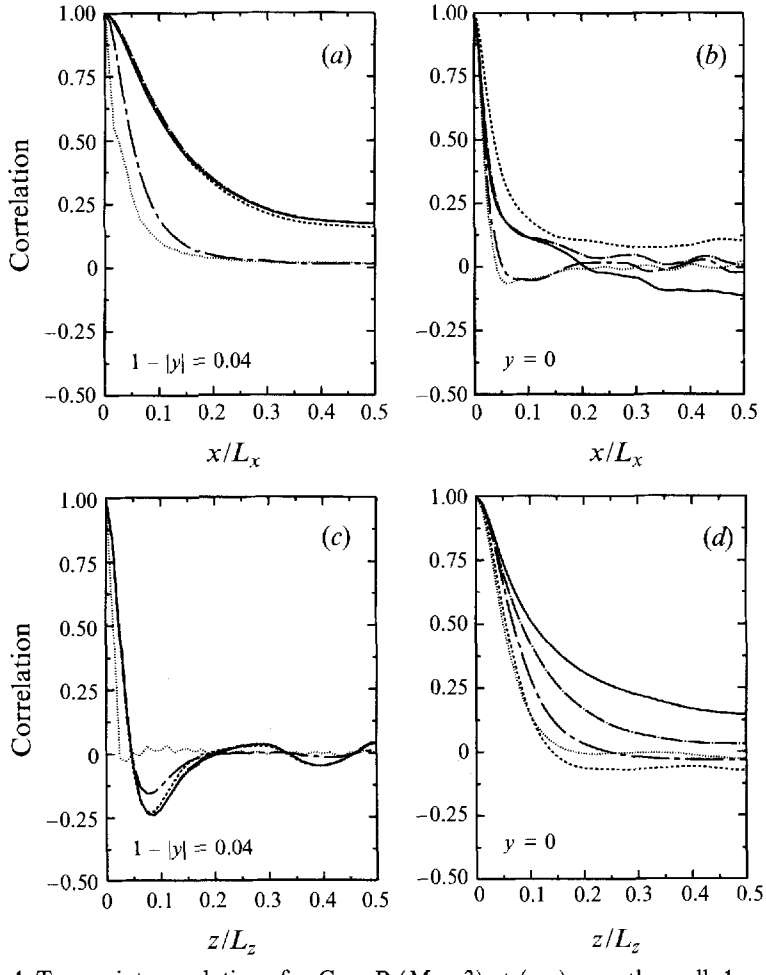

FIGURE 4. Two-point correlations for Case B ($M = 3$) at (a, c) near the wall, $1 - |y| = 0.04$, and (b, d) at the centreline: symbols as figure 1. (a, b) Streamwise; (c, d) spanwise.

(An average over six fields was taken, since it was not practical to perform the projection for the more than 25 fields used for the full average.) The solid curve shows the six-field average correlation before the eigenfunctions were removed. The magnitude of the reduction in the large-scale correlation in figure 5 suggests that the acoustic disturbances in the channel are primarily responsible for the large spanwise correlation. Note that because the computations assume that the channel walls are perfectly rigid (and use periodic boundary conditions), any acoustic signals present in the DNS are not expected to be identical to those found in laboratory wind tunnels, since in the simulations there is no mechanism by which the acoustic energy can radiate away. We shall see below, however, that the acoustic disturbances found here do not significantly affect the vorticity and entropy fields, especially near the walls.

The other difference, mentioned above, between the two-point correlations for the present and incompressible DNS is in the larger near-wall streamwise correlations found in figures 3(*a*) and 4(*a*); this indicates that the near-wall streaks, which are characteristic of wall-bounded turbulent flows (Robinson 1991), are more coherent

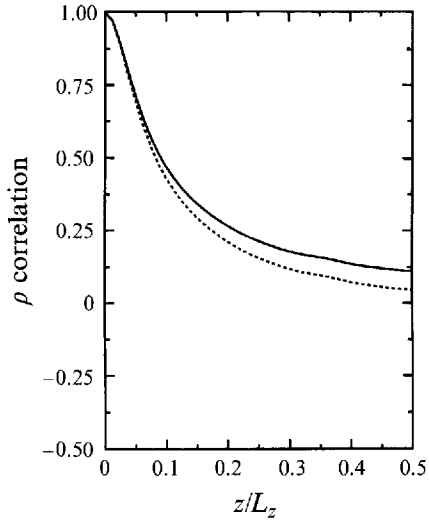

FIGURE 5. Two-point spanwise density correlations for Case A ($M = 1.5$) at the channel centreline: ——, average over six full DNS fields; - - - -, six-field average with acoustic eigenfunctions removed.

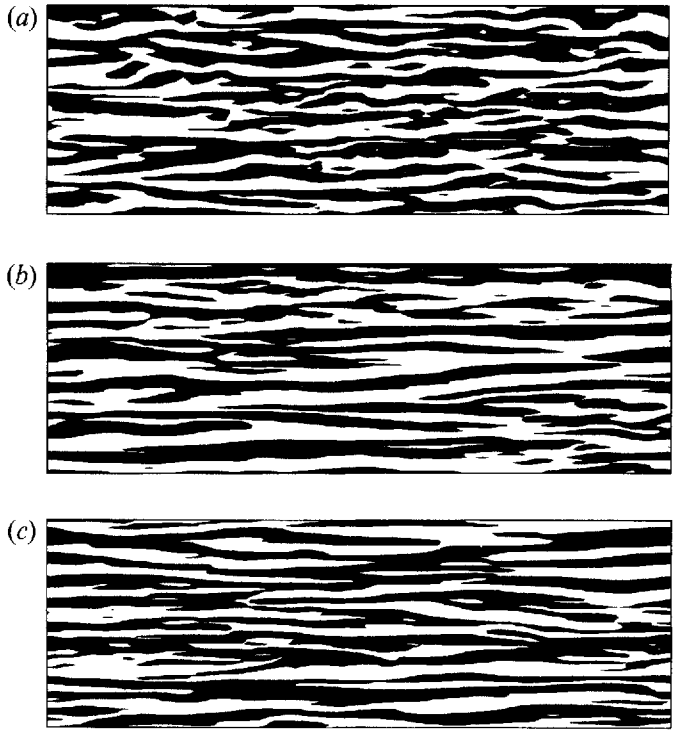

FIGURE 6. Contours of wall-normal vorticity on (x, z)-planes at $1 - |y| = 0.04$ for (a) incompressible channel, $M = 0$ (Kim *et al.* 1987), (b) Case A ($M = 1.5$), and (c) Case B ($M = 3.0$): ■, $\omega_y \leqslant 0$; □, $\omega_y > 0$. Flow from left to right; planes represent full flow domain.

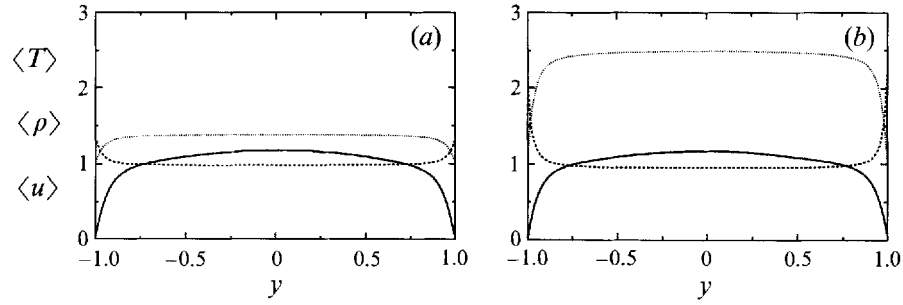

FIGURE 7. Mean profiles for (*a*) Case A ($M = 1.5$), and (*b*) Case B ($M = 3$): —, $\langle u \rangle$; - - - -, $\langle \rho \rangle$; · · · · ·, $\langle T \rangle$.

in Cases A and B than in the incompressible channel results.† The reason for the increased streamwise coherence will be taken up below. For now we note that the coherence increases with increasing Mach number (cf. figure 2 of Kim *et al.*, and figures 3*a* and 4*a*). This Mach number dependence is also apparent in figure 6, which illustrates the tendency for the contours of near-wall wall-normal vorticity from instantaneous fields at $M = 0$, 1.5 and 3 to become 'less wiggly' as the Mach number increases into the supersonic regime.

3.1.2. *Mean profiles*

Isothermal walls lead to qualitatively different mean-property variations than those found in adiabatic-wall boundary layers (see for example Fernholz & Finley 1977), since they allow the heat generated by the dissipation to be transferred out of the channel. The present and adiabatic cases thus differ in that here the walls are colder than the bulk of the flow and, instead of occurring at the walls, the maximum temperature and minimum density are found at the channel centreline. Furthermore, the maximum gradients of mean density and temperature are located at $y = \pm 1$. The mean flow is approximately isobaric, and the mean wall-normal pressure gradient is everywhere very small. For example, for both Cases A and B, $\gamma M^2 \mathrm{d}\langle p \rangle / \mathrm{d}y$ is always less than 0.5% of the product of the mean temperature gradient and mean density at the wall (recall $p = \rho T / \gamma M^2$, which implies $\mathrm{d}\langle p \rangle / \mathrm{d}y \approx (\langle \rho \rangle \mathrm{d}\langle T \rangle / \mathrm{d}y + \langle T \rangle \mathrm{d}\langle \rho \rangle / \mathrm{d}y) / \gamma M^2$). Figure 7 shows that as the Mach number increases so does the rate of heat transferred through the walls, and the near-wall density and temperature gradients consequently become increasingly steep. As we shall see below, these sharp near-wall mean gradients are a very important attribute of the isothermal-wall flow.

The profiles of local mean Mach number $\langle M \rangle = \langle u_{(y)} \rangle / \langle a_{(y)} \rangle$ (where $\langle a \rangle$ is the mean sound speed, equal to $\langle T \rangle^{1/2} / M$ in the current non-dimensionalization), for Cases A and B are given in figure 8(*a*). The 'sonic line' (i.e. the elevation at which the local Mach number is unity) is located at $1 - |y| = 0.115$ and 0.044, respectively. At $M = 1.5$, the mean centreline Mach number, $M_c = \langle u_c \rangle / \langle a_c \rangle$ ($\langle u_c \rangle$ and $\langle a_c \rangle$ are the mean values at the centreline), is also 1.5; at $M = 3$, however, $M_c = 2.2$ (recall that the bulk Mach number M is defined using the wall temperature). The 'friction Mach number' $M_\tau = u_\tau / \langle a_w \rangle$, where $\langle a_w \rangle$ is the sound speed based on the wall temperature

† It also implies that strictly speaking, near the walls the computational domain is too small in the streamwise direction, and that consequently the near-wall dynamics are not completely uninfluenced by the numerical parameters. This is not, however, thought to seriously affect any of the conclusions of this work.

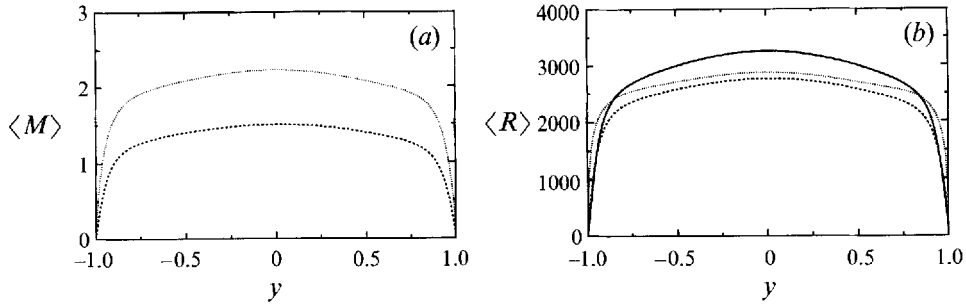

FIGURE 8. Local mean (*a*) Mach number $\langle M \rangle$ and (*b*) Reynolds number $\langle R \rangle$ profiles: ——, Kim *et al.* ($M = 0$); - - - -, Case A ($M = 1.5$); · · · · ·, Case B ($M = 3$).

Case	M_c	M_τ	Re_c	Re_τ	$-B_q$	$\langle \rho_w \rangle$	$\langle \rho_c \rangle$	$\langle T_c \rangle$	$\langle \mu_c \rangle$
Ref.†	0	0	3250	180	0	1	1	1	1
A	1.502	0.082	2760	222	0.049	1.355	0.980	1.378	1.252
B	2.225	0.116	2872	451	0.137	2.388	0.952	2.490	1.894
AX	1.742	0.095	3486	192	0.000	1.006	1.001	1.001	1.001

† Incompressible channel data of Kim *et al.* (1987).

TABLE 3. Time-averaged results.

and $Re\,\langle \rho_w \rangle u_\tau^2$ is the mean wall shear stress (w- and c-subscripts are used throughout to respectively denote values at the wall and the centreline), is 0.082 for Case A, and 0.116 for Case B. Another 'inner layer' parameter (which along with M_τ is assumed to uniquely determine the compressible law of the wall) is the non-dimensional heat flux, $B_q = (-1/Pr\,Re)(\mathrm{d}\langle T \rangle/\mathrm{d}y)_w/\langle \rho_w \rangle\, u_\tau$ (Bradshaw 1977). It is negative here, since the heat transfer is from the flow to the wall; $B_q = -0.049$ for Case A, and -0.137 for Case B, which respectively indicates moderate and strong cooling conditions (Huang & Coleman 1994). A summary of these and other time-averaged data for all the cases considered, including for reference Kim *et al.*'s (1987) $M = 0$ results, is given in table 3. For the sake of future modelling studies, we note that for both Mach numbers the mean viscosity $\langle \mu_c \rangle = \langle T_c^n \rangle$ is to an excellent approximation equal to $\langle T_c \rangle^n = \langle T_c \rangle^{0.7}$ (cf. Huang *et al.* 1995).

The variation with Mach number of the mean properties causes the bulk Reynolds number Re, and that based on the mean density, velocity and viscosity at the centreline, Re_c, to become increasingly different as the Mach number increases. The ratio of Re to Re_τ, the Reynolds number based on u_τ, $\langle \rho_w \rangle$ and $\langle \mu_w \rangle$, will also change with M, since $Re/Re_\tau = 1/\langle \rho_w \rangle u_\tau$. At first glance, it might therefore appear that this Re-dependence on Mach number could cause the near-wall streak modification mentioned above (i.e. extra streamwise coherence with increasing M) by lowering the Reynolds number and making the streamwise domain size smaller when measured in wall units. To address this question we examine how the variation across the channel of $\langle R \rangle$, the local mean Reynolds number based on $\langle \rho_{(y)} \rangle$, $\langle u_{(y)} \rangle$ and $\langle \mu_{(y)} \rangle$, changes with Mach number. Figure 8(*b*) indicates that the centreline Reynolds number is indeed higher in the incompressible DNS than that found here: the $M = 1.5$ centreline value (2760) is less than the 3250 quoted for the Kim *et al.* (1987) incompressible channel data (compare the dotted and solid curves). However, for the isothermal-wall flow the maximum mean temperature and minimum mean density – and therefore

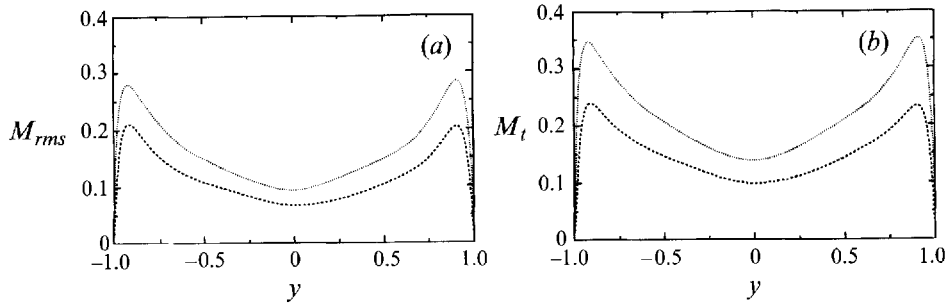

FIGURE 9. Fluctuation Mach number profiles: - - - -, Case A ($M = 1.5$); · · · · ·, Case B ($M = 3$). (*a*) $M_{rms} = \langle (m - \langle m \rangle)^2 \rangle^{1/2}$, and (*b*) $M_t = q/\langle a \rangle$, where $m = (u_i u_i)^{1/2}/a$, $q^2 = \langle u_i' u_i' \rangle$, and $a = T^{1/2}/M$.

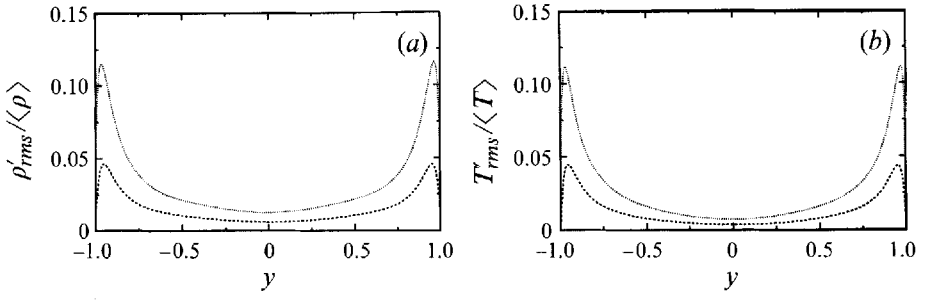

FIGURE 10. RMS fluctuations of (*a*) density and (*b*) temperature: - - - -, Case A ($M = 1.5$); · · · · ·, Case B ($M = 3$).

the maximum mean kinematic viscosity $\langle \mu \rangle / \langle \rho \rangle$ – occur at the centerline. The local Reynolds number in the present DNS is thus larger near the walls than when ν = constant. This suggests that the enhanced near-wall coherence is a Mach number (or heat transfer) effect, and not due to Reynolds number differences *per se*, a fact that is reinforced by the Case B results. In order to obtain a local Reynolds number profile for $M = 3$ that is similar to that for Case A, the bulk Reynolds number was increased from 3000 to 4880. As the Case B profile (dotted curve) in figure 8(*b*) shows, $\langle R \rangle$ at any y is slightly larger than that for Case A. Changing Re causes the domain size in wall units, L_x^+ and L_z^+ respectively, to increase from $L_x^+ = 2790$ and $L_z^+ = 930$ for Case A to 5670 and 1890 for Case B. (For the incompressible DNS, Kim *et al.* used $(L_x^+, L_z^+) = (2300, 1150)$.) Therefore, the further increase of the near-wall streamwise correlations associated with the change from $M = 1.5$ to 3 (cf. figures 3*a* and 4*a*) is not a viscous effect.

Fairly large r.m.s. Mach numbers are found for both cases, especially near the walls, where for $M = 3$ the maximum value approaches 0.3 (figure 9*a*). The 'turbulent Mach number', $M_t = q/\langle a \rangle$ ($q^2 = \langle u_i' u_i' \rangle$), exhibits the same general behaviour as M_{rms}, although figure 9(*b*) shows that it is consistently larger. The difference between the two, which is greatest for Case B, where the near-wall peak in M_t is about 25% larger than that for M_{rms}, points to a significant non-zero velocity–temperature correlation.

The large density and temperature fluctuations associated with the near-wall M_t are illustrated in figure 10. Although both have r.m.s. values near the wall that are greater than 10% of their means, the joint probability density functions (p.d.f.) shown in figure 11 suggest that these disturbances are mostly of a non-acoustic nature, primarily the result of solenoidal 'passive mixing' across a mean gradient. The density–temperature and velocity–temperature p.d.f.s were taken from a single Case B

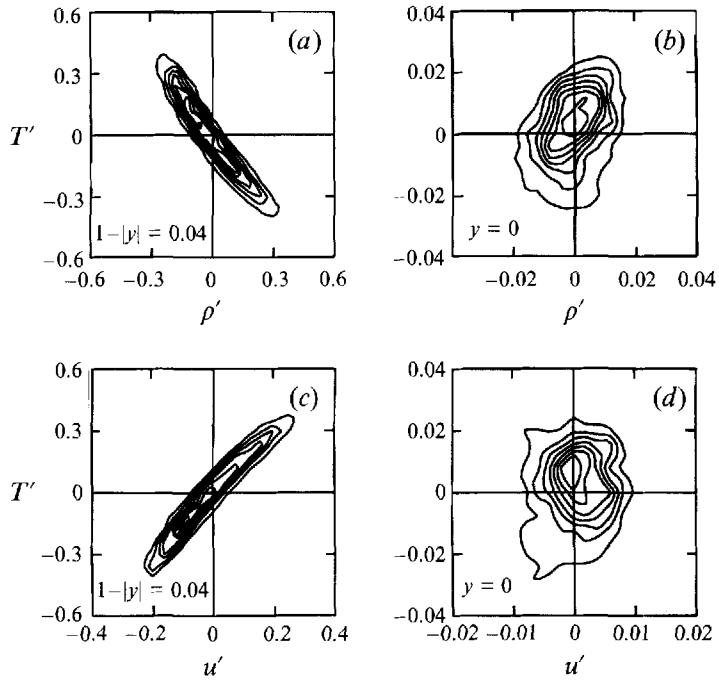

FIGURE 11. Joint probability densities of (a, b) density *vs.* temperature, and (c, d) streamwise velocity *vs.* temperature for Case B ($M = 3$): (a, c) Near the wall ($1 - |y| = 0.04$); (b, d) at the centreline.

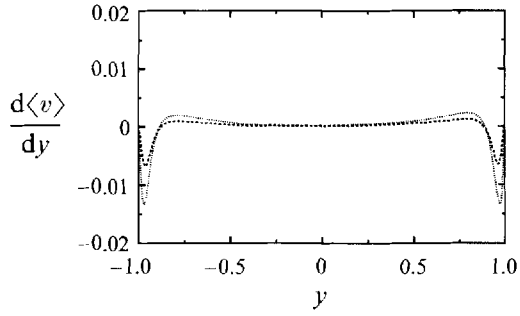

FIGURE 12. Mean dilatation: - - - -, Case A ($M = 1.5$); · · · · ·, Case B ($M = 3$).

realization, near a wall ($1 - |y| = 0.04$) and at the centreline. Note the strong negative ρ–T and positive u–T correlations near the wall, which one would also find if the density and temperature were passive scalars with mean gradients as shown in figure 7. On the other hand, if the density–temperature interaction were purely isentropic, $T' \sim (\gamma - 1)\rho'$, then $\langle \rho' T' \rangle$ would be positive. Near the centreline (figure 11*b*), where $d\langle\rho\rangle/dy$ and $d\langle T\rangle/dy \approx 0$, the ρ–T correlation indicates (since it is greater than zero, though small) that the flow is more nearly isentropic, as the acoustic eigenfunction analysis discussed above suggests.

There are some non-solenoidal effects however, that occur near the walls. Figure 12 reveals that the mean dilatation within the channel is not zero, and the maximum compression (which strengthens with Mach number) occurs at about $1 - |y| = 0.03$. Between $-0.9 < y < 0.9$ a weaker fairly uniform mean expansion occurs. The dilatation associated with the turbulent fluctuations is weaker

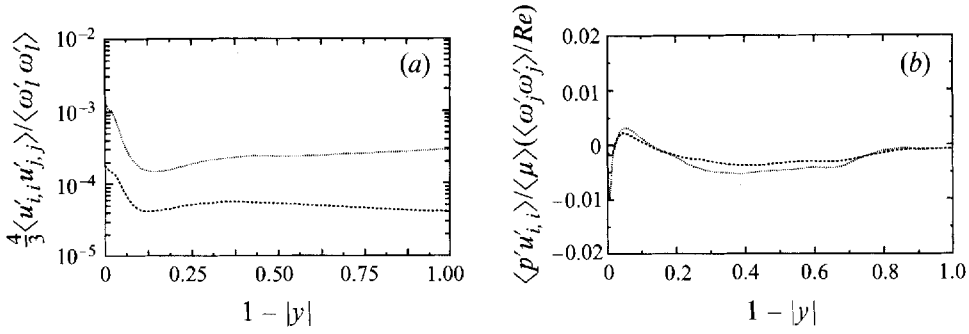

FIGURE 13. Profiles of (*a*) dilatation-to-enstrophy and (*b*) pressure–dilatation correlation ratios: - - - -, Case A ($M = 1.5$); · · · · ·, Case B ($M = 3$).

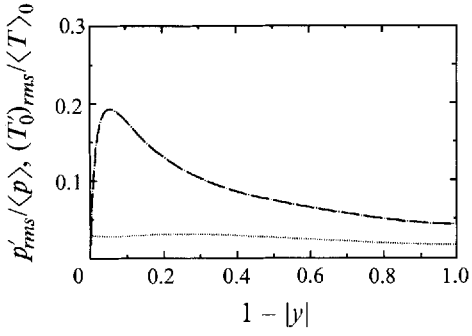

FIGURE 14. Pressure and total temperature fluctuations for Case B ($M = 3$): · · · · ·, p'; —·—, T'_0.

still. It is not, for example, important enough to directly increase the turbulent kinetic energy dissipation rate to any great degree. This can be seen from figure 13(*a*), which gives the ratio of the mean-square dilatation fluctuations to those of the mean-square vorticity: the ratio of dilatational-to-solenoidal homogeneous kinetic energy dissipation (Zeman 1990; Speziale & Sarkar 1991; Lele 1994). While the ratio increases by an order of magnitude as M increases from 1.5 to 3, it never becomes significantly larger than 10^{-3}. The other source term introduced into the turbulent kinetic energy transport equation by the compressibility, the pressure-dilatation correlation, is also found to be negligible (figure 13*b*). It is never greater than 1% of the (homogeneous) solenoidal dissipation anywhere in the flow.† The ability of some recently proposed dilatational–dissipation and pressure-dilation models to reproduce the above results is considered in Huang *et al.* (1995).

With such small dilatational effects present, one might surmise that this flow is governed well by Morkovin's (1964) hypothesis, which states that relationships between (relevant) statistical properties of turbulence are unaffected by compressibility if the r.m.s. density fluctuations are small (of order 1/10) compared to the absolute density (Bradshaw & Ferriss 1971; Bradshaw 1977; Spina *et al.* 1994). The density fluctuations for both Mach numbers are within the allowed range of $O(1/10)$ (figure 10*a*), but since Morkovin's hypothesis does not claim to account for the influence

† Because the mean dilatation was mistakenly not removed from the $\langle p'u'\rangle_{i,i}$ correlation shown in figures 10 and 16 of Coleman (1993), it was erroneously claimed in that report that this term was significant.

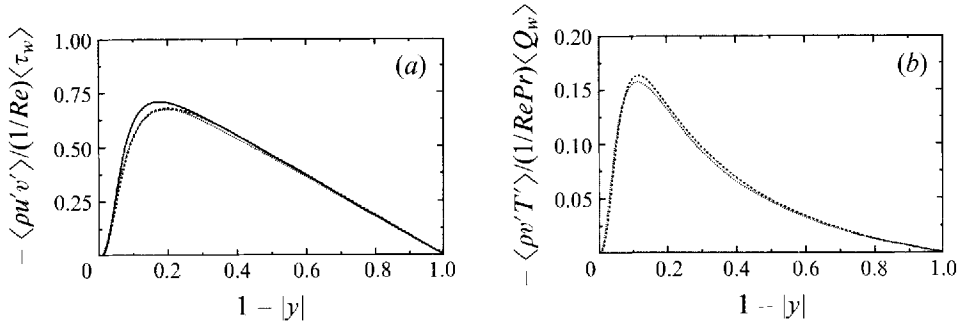

FIGURE 15. Profiles of (*a*) Reynolds shear stress and (*b*) turbulent heat flux: ——, Kim *et al.* ($M = 0$); - - - -, Case A ($M = 1.5$); · · · · ·, Case B ($M = 3$). The wall values are $\langle\tau_w\rangle = (\mathrm{d}\langle u\rangle/\mathrm{d}y)_w$ and $\langle Q_w\rangle = (\mathrm{d}\langle T\rangle/\mathrm{d}y)_w$

of spatial gradients of mean properties (Bradshaw 1977), which are important here, the ρ' criterion cannot be accepted as conclusive. Morkovin's original conjecture is that at non-hypersonic Mach numbers, acoustic pressure fluctuations and variations of total temperature are negligible. It therefore follows that a more rigorous test of his hypothesis is to examine the magnitude of the pressure and total temperature fluctuations with respect to their means; this is done in figure 14, for the $M = 3$ case. Both the r.m.s. fluctuations of pressure p and total temperature $T_0 = T + \frac{1}{2}(\gamma-1)M^2 u_i u_i$ are much less than their mean values – with the former a much smaller percentage of its mean than the latter. Because of the non-zero heat transfer through the walls, the total temperature fluctuations are larger than those found near adiabatic walls. The $M = 1.5$ profiles (not shown) exhibit similar behaviour, with the p' and T_0' curves each about half as large as the $M = 3$ results. The $p'/\langle p\rangle \ll 1$ criterion is certainly met, with maximum r.m.s. values everywhere less than about 3%. And since the peak r.m.s. T_0' is only about 20% of $\langle T_0\rangle$, the total temperature requirement is also fairly well satisfied. (Note that the r.m.s. $T'/\langle T\rangle$ maximum is only about half that for the total temperature; figure 10*b*.) The implications of the flow only approximately satisfying $T_0'/\langle T_0\rangle \ll 1$ upon Morkovin's 'strong Reynolds analogy' – which is derived by assuming T_0 is constant – is explored in Spina *et al.* (1994) and Huang *et al.* (1995).

We thus expect that there is a good chance that Morkovin's hypothesis regarding the invariance to Mach number of relevant statistical ratios will be valid for the present results. Indeed, for at least two important statistical ratios, the Reynolds-to-wall-shear stress ratio, $\langle\rho u'v'\rangle/(1/Re)\langle\tau_w\rangle$, and the turbulent-to-wall heat flux ratio, $\langle\rho v'T'\rangle/(1/RePr)\langle Q_w\rangle$, it is found to work very well. Figures 15(*a*) and 15(*b*), which contrast the Case A and B data with each other, and for the shear stress with Kim *et al.*'s (1987) incompressible channel statistics, demonstrate that both quantities are reasonably independent of Mach number. That the Case A and B Reynolds stress profiles have a lower maximum than the incompressible results (figure 15*a*) is probably due to the slightly lower effective Reynolds number of the present DNS. Two other statistical ratios found to be approximately independent of Mach number, and to agree with their incompressible counterparts, are the mixing length $(-\langle u'v'\rangle)^{1/2}/(\mathrm{d}\langle u\rangle/\mathrm{d}y)$ and the Reynolds-shear-stress correlation coefficient; they are shown in figure 16. There is a slight increase with M of the near-wall maximum of $|\langle u'v'\rangle|/u'_{\mathrm{rms}}v'_{\mathrm{rms}}$ in figure 16(*b*) (and a slight decrease with M for $1-|y| > 0.1$), but

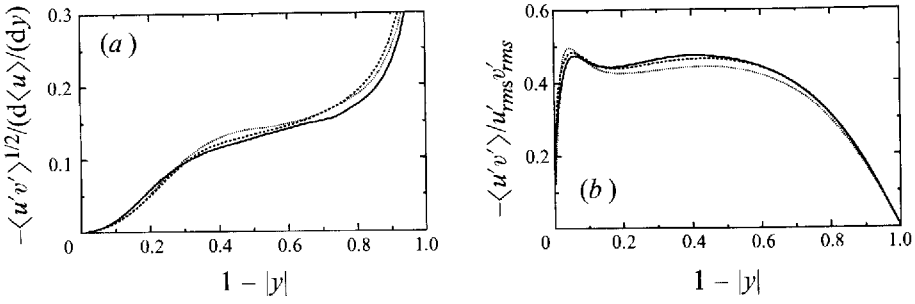

FIGURE 16. Profiles of (*a*) mixing length and (*b*) Reynolds stress correlation: ——, Kim *et al.* ($M = 0$); - - - -, Case A ($M = 1.5$); · · · · ·, Case B ($M = 3$).

the magnitude is almost certainly statistically insignificant† and not related to the enhanced streak coherence mentioned above.

With the invariance of the mixing length established (figure 16*a*), the so-called Van Driest transformation for the mean velocity immediately follows. That is, the density-weighted mean velocity

$$\langle u\rangle^+_{VD} = \int_0^{\langle u\rangle^+} \left(\frac{\langle\rho\rangle}{\langle\rho_w\rangle}\right)^{1/2} \mathrm{d}\langle u\rangle^+ \tag{6}$$

(where $\langle\rho_w\rangle$ is the mean density at the wall and the + superscript denotes wall units given by $\langle\tau_w\rangle$, $\langle\rho_w\rangle$ and $\langle\mu_w\rangle$), is expected to satisfy the incompressible log law,

$$\langle u\rangle^+_{VD} = \frac{1}{\kappa}\ln y^+ + C, \tag{7}$$

with κ and C similar to their incompressible values, $\kappa \approx 0.41$, and $C \approx 5.2$ (Bradshaw 1977; Huang, Bradshaw & Coakley 1993; Huang & Coleman 1994). The wall-unit and Van Driest transformation (6) forms of the mean velocity are plotted in figures 17(*a*) and 17(*b*), respectively. The figure 17(*b*) results are very similar to those shown in figure 1(*b*) of Huang & Coleman (1994), which were obtained by using a mixing-length formulation for the temperature to write $\langle u\rangle^+_{VD}$ as a function of only $\langle u\rangle^+$, the surface heat flux and the mean surface temperature (i.e. utilizing equation (7) of Bradshaw (1977)). (The Huang & Coleman paper also presents a mixing-length scheme generalized to simultaneously account for the viscous and log-law regions.) The agreement of the curves in figure 17(*b*), especially their slopes (see Huang & Coleman 1994), reinforces the validity for this flow of the Van Driest transformation and, by implication, that of the Morkovin hypothesis.

The importance of properly accounting for the mean property variations in the near-wall scaling can be seen in figures 18 and 19. When normalized by conventional wall variables (defined in terms of the mean density, viscosity and shear stress at the wall), the differences between the non-zero-M and incompressible r.m.s. velocity and vorticity fluctuation profiles increase with Mach number (figures 18*a* and 19*a*). But when the 'semi-local' scaling suggested by Huang *et al.* (1995) is used instead (replacing $\langle\rho_w\rangle$ with $\langle\rho_{(y)}\rangle$, $\langle\mu_w\rangle$ with $\langle\mu_{(y)}\rangle$, and u_τ with $u^*_{\tau(y)} = (\langle\tau_w\rangle/\langle\rho_{(y)}\rangle Re)^{1/2}$; recall that $(\langle\tau_{12}\rangle - Re\langle\rho u'v'\rangle)/\langle\tau_w\rangle \approx |y|$ and see Huang *et al.* (1995)), the collapse is much better, for both velocity and vorticity. Antonia & Kim (1994) have shown that for incompressible boundary layers, only the y-component of vorticity is independent

† The larger increase in the near-wall value presented in Coleman (1993) was the result of assuming $\langle v\rangle = 0$, and is therefore incorrect.

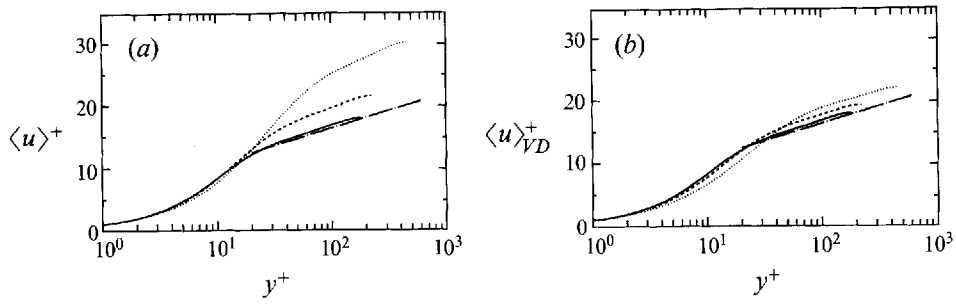

FIGURE 17. Mean streamwise velocity: —, Kim *et al.* ($M = 0$); - - - -, Case A ($M = 1.5$); · · · · ·, Case B ($M = 3$); — · —, $2.44 \ln y^+ + 5.2$. (*a*) In wall units; (*b*) with Van Driest transformation (6).

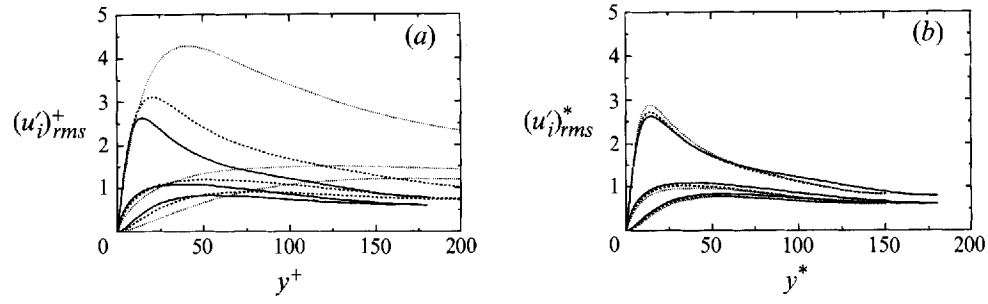

FIGURE 18. RMS velocity fluctuations: —, Kim *et al.* (1987) ($M = 0$); - - - -, Case A ($M = 1.5$); · · · · ·, Case B ($M = 3$). (*a*) In wall units, and (*b*) in semi-local coordinates. Wall variables y^+ and $(u_i')^+_{rms}$ based on $\langle\rho_w\rangle$, $\langle\mu_w\rangle$ and $u_\tau = (\langle\tau_w\rangle/Re\,\langle\rho_w\rangle)^{1/2}$; semi-local quantities y^* and $(u_i')^*_{rms}$ non-dimensionalized by $\langle\rho_{(y)}\rangle$, $\langle\mu_{(y)}\rangle$ and $u^*_{\tau(y)} = (\langle\tau_w\rangle/Re\,\langle\rho_{(y)}\rangle)^{1/2}$. Upper, middle and lower curves denote u, w and v, respectively.

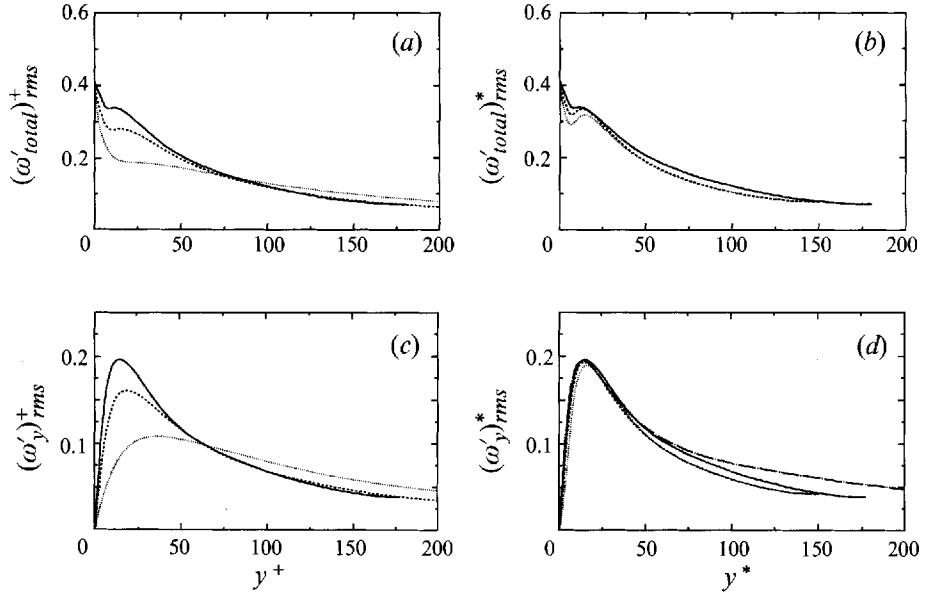

FIGURE 19. Profiles of (*a*, *b*) total and (*c*, *d*) wall-normal RMS vorticity fluctuations: symbols as figure 18; — · —, Antonia & Kim (1994) ($Re_c = 7890$, $M = 0$) for (*d*). (*a*, *c*) In wall units, and (*b*, *d*) in semi-local coordinates. Total vorticity fluctuations given by $(\omega'_{total})_{rms} = \langle\omega_i'\omega_i'\rangle^{1/2}$.

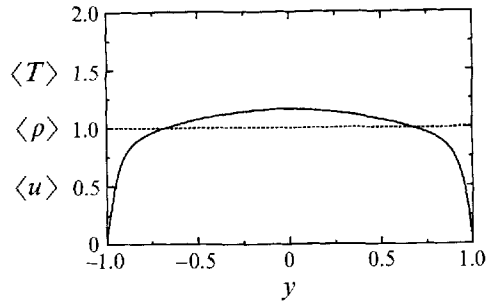

FIGURE 20. Mean profiles for Case AX ($M = 1.5$, $M_d = 0$): —, $\langle u \rangle$; - - - -, $\langle \rho \rangle$; · · · · ·, $\langle T \rangle$ ($\langle \rho \rangle$ and $\langle T \rangle$ coincident).

of Re when normalized by the wall values. Since the Case A and B profiles in figures 19(c) and 19(d) agree well with $M = 0$ results for two Re (the solid and chain-dotted curves in figure 19(b) represent the incompressible $Re_c = 3250$ and 7890 DNS data of Kim *et al.* (1987) and Antonia & Kim (1994), respectively), this scaling of ω_y preserves the Reynolds number invariance while also being independent of Mach number. The semi-local scaling for the friction velocity is valid here because the ratio of the local- to wall-shear stress is insensitive to M (figure 15a); it is therefore expected that a fully local scheme that replaced $\langle \tau_w \rangle$ in the above definition of $u^*_{\tau(y)}$ with $\langle \tau_{total(y)} \rangle = \langle \tau_{12} \rangle - Re \langle \rho u' v' \rangle$ would also be effective.

Note that the successful use of y^+, instead of y^*, in the Van Driest transformation in figure 17(b) is not inconsistent with the semi-local scaling. The invariance of the mixing-length profiles (see figure 16a) – from which the Van Driest mapping is derived (Bradshaw 1977) – implies that if the mixing length is κy and $-\langle u'v' \rangle \approx \langle \tau_w \rangle / \langle \rho \rangle Re$ (both key assumptions in the development of the Van Driest transformation), the mean shear in the semi-local normalization $(\mathrm{d}\langle u \rangle / \mathrm{d}y)^* \equiv (\mathrm{d}\langle u \rangle / \mathrm{d}y) / (\langle \rho \rangle u^{*2}_\tau / \langle \mu \rangle)$ is given by $1/\kappa y^*$. It can also be shown that as y^* increases $(\mathrm{d}\langle u \rangle / \mathrm{d}y)^*$ approaches $\mathrm{d}\langle u \rangle^* / \mathrm{d}y^*$, so that for sufficiently large y^*, $\langle u \rangle^* \approx (1/\kappa) \ln y^* + C^*$, where C^* is a different constant from that in (7) that will in general depend on the heat transfer and shear (i.e. B_q and M_τ) at the wall.

3.2. *Simulation with extra source* ($\mathscr{S} \neq 0$)

The main motivation for the run described in this section, Case AX, is to determine the influence of the property variations on the behaviour (i.e. increased streamwise coherence with Mach number) of the near-wall streaks. Consequently, for this $M = 1.5$ simulation the 'dissipation Mach number' (see §2) is set to $M_d = 0$, so that the non-zero temperature equation sink $\mathscr{S}$ (5) yields a mean density and temperature that are constant (figure 20). Besides these mean profile differences, the fluctuation fields are also quite different from their $M = M_d$ counterparts. To begin with, they are much weaker, with maximum r.m.s. ρ' and T' only about 40% and 15% as large, respectively, as those found for Case A (contrast figures 10 and 21). Furthermore, as one would expect for a flow with no mean heat transfer through the walls, the density and temperature fluctuations are approximately isentropic. If they were exactly so, the solid curve in figure 21 – which represents the isentropic temperature field associated with the density disturbances – would exactly coincide with the dashed profile, the actual r.m.s. temperature. As it is, the two are fairly close, especially near the channel centreline. A more straightforward indication of the isentropic ρ–T relationship is given by the p.d.f.s in figure 22. The axes are scaled so that the isentropic state,

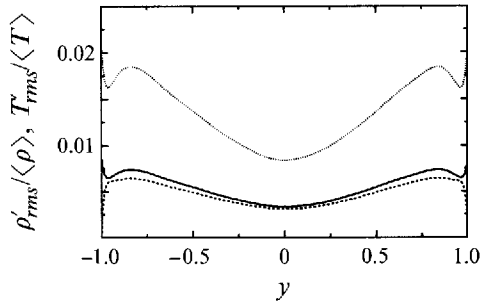

FIGURE 21. RMS density and temperature profiles for Case AX ($M = 1.5$, $M_d = 0$): - - - -, T'; · · · · ·, ρ'; ——, $(\gamma - 1)\rho'_{rms}/\langle\rho\rangle$.

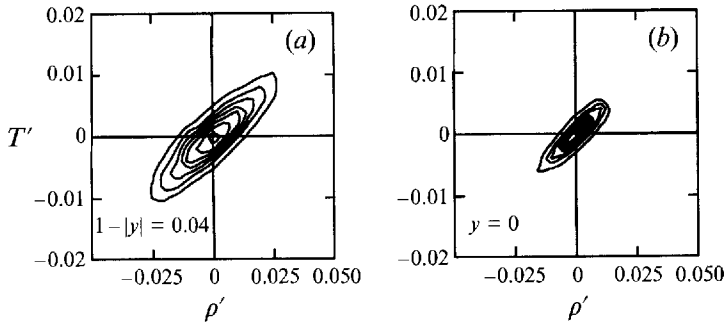

FIGURE 22. Joint probability densities of density *vs.* temperature for Case AX ($M = 1.5$, $M_d = 0$): (*a*) Near wall ($1 - |y| = 0.04$); (*b*) at the centreline.

$\rho'/\langle\rho\rangle = (\gamma - 1)T'/\langle T\rangle$, lies along the diagonal connecting the lower-left with the upper-right corners of the plot. The p.d.f. contours for both locations imply that uniform-mean Case AX flow is to a good approximation isentropic.

The near-wall streamwise correlations for Case AX are given in figure 23. No indication of the enhanced streak coherence found for Cases A and B is observed (cf. figures 3*a* and 4*a*), and in fact the correlations are very close to those observed at $M = 0$ (see figure 2 of Kim *et al.*). This leads us to perhaps the most significant conclusion of this section: non-zero wall-normal gradients of mean properties are required for the streak modification to occur. An explanation of this observation is found in figure 24, which compares profiles of $S^* \equiv \langle\rho\rangle Sq^2/\langle\mu\rangle\langle\omega'_i\omega'_i\rangle$ for the three compressible cases, A, B and AX, with the $M = 0$ result. This quantity represents the ratio of a turbulent timescale, $\langle\rho\rangle q^2/\langle\mu\rangle\langle\omega'_i\omega'_i\rangle$, to that of the mean strain, $S^{-1} = (\frac{1}{2}\mathrm{d}\langle u\rangle/\mathrm{d}y)^{-1}$. Although it is common to use $\varepsilon = 2\langle\mu\rangle\langle s'_{ij}s'_{ij}\rangle/\langle\rho\rangle$ (where $s'_{ij} = \frac{1}{2}(u'_{i,j} + u'_{j,i})$) to define the turbulent timescale, the choice used here is also valid, since ε (which for incompressible flows is equivalent to the rate of turbulent kinetic energy dissipation) and $\langle\mu\rangle\langle\omega'_i\omega'_i\rangle/\langle\rho\rangle$ have the same units and differ by at most three or four percent (see Huang *et al.* 1995). We find that as the Mach number increases, and the mean property variations become more extreme, the maximum timescale ratio increases from about 18 at $M = 0$ to nearly 28 at $M = 3$. The same tendency to increase with M is also found when ε is used to represent the turbulent timescale, and for the shear-to-vorticity ratio S/ω'_{rms} (not shown). The agreement of the $M_d = 0$ (Case AX) and $M = 0$ profiles (the chain-dotted and solid curves) indicates that the increase of the timescale ratio is due to changes of the mean density and temperature.

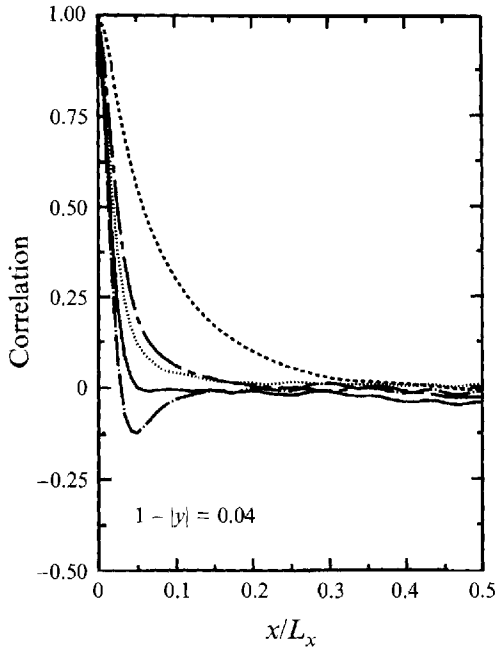

FIGURE 23. Two-point correlations near the wall at $1 - |y| = 0.04$ for Case AX ($M = 1.5$, $M_d = 0$): symbols as figure 1.

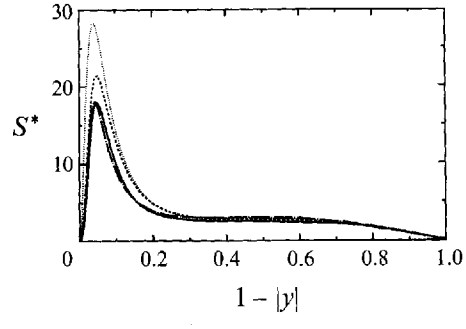

FIGURE 24. Profiles of $S^* = \frac{1}{2}Re\langle\rho\rangle(\mathrm{d}\langle u\rangle/\mathrm{d}y)q^2/\langle\mu\rangle\langle\omega_i'\omega_i'\rangle$: ——, Kim *et al.* (1987) ($M = 0$); - - - -, Case A ($M = 1.5$); · · · · ·, Case B ($M = 3$); — · —, Case AX ($M = 1.5$, $M_d = 0$).

This fact, coupled with the observation that in homogeneous shear flow turbulent 'eddies' become increasingly elongated in the streamwise direction as S^* increases† (Lee, Kim & Moin 1990) suggests that the enhanced streamwise coherence of the near-wall streaks found above is caused by the change of the turbulence-to-mean timescale ratio by the mean property variations.

† Note also that although in general it is possible for S^* to become so large that its magnitude becomes irrelevant, Lee *et al.*'s results indicate that the peak value of S^* in turbulent boundary layers is not large enough that changes in the magnitude of the near-wall maximum have no effect (see their figure 14, for example, which compares evolution of the correlation length given by their DNS with that predicted by rapid distortion theory). And while a non-stationary homogeneous shear flow and a stationary non-homogeneous boundary layer are not expected to exactly correspond, the tendency in Lee *et al.*'s simulations for the asymptotic long-time 'shape' of eddies to be determined by the shear rate (see their figure 15) is taken as further evidence that the modification of near-wall streaks observed here is the result of changes in S^*.

While searching for an explanation of the streak modification, another possibility was considered, in addition to that just presented. It assumed an analogy between the streamwise coherence of the streaks and the stability of compressible shear layers. That is, the region of high wall-normal vorticity between the high- and low-speed streaks was interpreted as a shear layer, and a compressibility mechanism responsible for increased stability was sought, with the increased stability being associated with the extra streamwise coherence. This approach was prompted by the large positive correlation between u and T near the walls, and in particular the fact that the low-speed streaks tend to be coldest and therefore have highest density (see figure 11*a*, *c*). The resulting variable-density 'mixing layer' at the edge of a cold low-speed streak was thought perhaps to be governed by the same dynamics responsible for the reduced spreading rates of compressible shear layers found by, for example, Brown & Roshko (1974), Papamoschou & Roshko (1986, 1988), Lele (1989) and Sandham & Reynolds (1991). In the present results it was observed that significant dilatational perturbations are focused along the cold low-speed streaks near the walls; that is, their lower sound speed caused the cold streaks to act as 'acoustic wave guides.' However, since the focused dilatational fluctuations propagate along the low-speed streaks at (locally) supersonic speeds, while vorticity fluctuations move much more slowly, any tendency for them to affect ω_y is probably slight – presumably any stabilizing influence is quickly followed by a destabilizing effect. Moreover, the maximum instantaneous 'convective Mach number' M_c (the ratio of the velocity difference to the sum of the 'free-stream' sound speeds) across the edge of the cold streak for Case B is only about 0.3. This quantity has been found to provide a good parameterization of compressibility effects on mixing-layer growth rates (Papamoschou & Roshko 1988), and significant compressibility effects are not seen experimentally until $M_c > 0.5$ (Papamoschou & Roshko 1986, 1988). We therefore conclude that the acoustic wave-guide phenomenon is a dynamically insignificant, passive effect, and acoustic stabilization is not significant in the streaks. It may, however, be important at Mach numbers higher than those considered here.

4. Summary and concluding remarks

DNS results for fully developed, isothermal-wall, compressible channel flow for Mach numbers, based on bulk velocity and wall sound speed, up to 3 have been obtained. These results, when properly scaled to account for mean property variations, agree in many ways with the incompressible DNS data of Kim *et al.* (1987). The Morkovin hypothesis, and the resultant Van Driest transformation, are found on the whole to be very successful, although the requirement that instantaneous total temperature remain constant is only approximately satisfied.

The isothermal-wall flow is strongly influenced by sharp gradients of mean density and temperature that occur near the walls, to the point that most of the ρ and T fluctuations are the result of solenoidal 'passive mixing' of the temperature and density by the turbulence. Results found here are therefore not expected to be identical to those found for the adiabatic-wall case. Large-scale acoustic disturbances are observed to span the channel. While they are an important part of the density and temperature fluctuations near the centreline, these disturbances do not significantly affect the velocity field, especially near the walls (cf. Kovásznay 1953). The only 'non-Morkovin' phenomenon of note, in the sense that the 'structure' of the turbulence is modified, is an increase with Mach number of the streamwise coherence of the near-wall streaks. But instead of representing an exception to Morkovin's postulate that

only mean property variations (and not thermodynamic fluctuations) are important at supersonic Mach numbers, the enhanced streak coherence ultimately has its source in the mean property variations, since they act to alter the relationship between the mean and turbulent timescales near the walls. Paradoxically, the modified structure of the streaks actually reinforces Morkovin's hypothesis instead of contradicting it.

The scheme introduced by Buell (1991) for differentiating between compressibility effects due to thermodynamic fluctuations and those caused by mean property variations, using an effective heat source defined by a 'dissipation Mach number', was found to be a valuable tool. This approach, which was here employed to created a $M = 1.5$ flow with constant density and temperature profiles, has a wide potential application, and should be useful for other flow configurations and at higher Mach numbers.

The first author was supported by the Stanford/NASA-Ames Center for Turbulence Research during the course of this study. Computations were performed on the ACF and NAS computers at NASA-Ames Research Center. Most of the codes used in this work were developed by Dr J. C. Buell. We have also greatly benefited from advice and valuable suggestions given by Professors P. Bradshaw, J. H. Ferziger, S. K. Lele and the late Dr O. Zeman. Finally, a special note of thanks is due Dr P. G. Huang: his involvement in this project is deeply appreciated.

Appendix. Determination of acoustic eigenfunctions

The 'acoustic extraction' discussed in §3.1 is done by projecting the DNS fields on eigenfunctions of the linear inviscid isentropic equations for a given parallel base flow. That is, the density, velocity and pressure eigenfunctions are assumed to satisfy

$$\frac{\partial \rho'}{\partial t} + \overline{u}\frac{\partial \rho'}{\partial x} + v'\frac{\partial \overline{\rho}}{\partial y} + \overline{\rho}\frac{\partial u_j'}{\partial x_j} = 0, \tag{A1a}$$

$$\frac{\partial u_i'}{\partial t} + \overline{u}\frac{\partial u_i'}{\partial x} + v'\frac{\partial \overline{u_i}}{\partial y} + \frac{1}{\overline{\rho}}\frac{\partial p'}{\partial x_i} = 0, \tag{A1b}$$

$$p' - \overline{T}\,\rho'/M^2 = 0, \tag{A1c}$$

where $\overline{v} = \overline{w} = 0$ and $\overline{\rho}$, $\overline{u}$ and $\overline{T}$ vary in y only. The isentropic relation (A1c) is invoked in order to limit attention only to 'purely acoustic' disturbances; the need for this assumption and its implications is discussed below.

After substituting (A1c) into (A1b), and using a Fourier representation for the density and velocity fluctuations, such that $\rho'(\boldsymbol{x},t) = \sum_{\boldsymbol{k}} \widehat{\rho}(\boldsymbol{k},y)\exp[\mathrm{i}(\boldsymbol{k}\cdot\boldsymbol{x} - \omega t)]$ and $u_i'(\boldsymbol{x},t) = \sum_{\boldsymbol{k}} \widehat{u}_i(\boldsymbol{k},y)\exp[\mathrm{i}(\boldsymbol{k}\cdot\boldsymbol{x} - \omega t)]$, the linearized, isentropic Euler equations in Fourier space at a given wavenumber $\boldsymbol{k} = (k_x, k_z)$ can be written in terms of the 'acoustic eigenfunctions' $\boldsymbol{q}_\ell(\boldsymbol{k},y) = (\widehat{\rho}(\boldsymbol{k},y), \widehat{u}(\boldsymbol{k},y), \widehat{v}(\boldsymbol{k},y), \widehat{w}(\boldsymbol{k},y))_\ell^{\mathrm{T}}$ as $\mathscr{L}(\boldsymbol{q}) = \omega\boldsymbol{q}$, where

$$\mathscr{L}(\boldsymbol{q}) = \begin{pmatrix} k_x\overline{u}\,\widehat{\rho} + k_x\overline{\rho}\,\widehat{u} - \mathrm{i}\mathrm{d}(\overline{\rho}\,\widehat{v})/\mathrm{d}y + k_z\overline{\rho}\,\widehat{w} \\ k_x\overline{u}\,\widehat{u} - \mathrm{i}(\mathrm{d}\overline{u}/\mathrm{d}y)\widehat{v} + k_x\overline{a}\,\widehat{\rho}/\overline{\rho} \\ k_x\overline{u}\,\widehat{v} - \mathrm{i}\overline{a}\,\mathrm{d}(\widehat{\rho}/\overline{\rho})/\mathrm{d}y \\ k_x\overline{u}\,\widehat{w} + k_z\overline{a}\,\widehat{\rho}/\overline{\rho} \end{pmatrix}, \tag{A2}$$

and $\overline{a} = \overline{T}/M^2$ is the base-flow sound speed, with $\widehat{v} = 0$ at $y = \pm 1$.

The projection of the full DNS field onto the acoustic subspace is performed by computing the inner product $\int_{-1}^{+1} \boldsymbol{q}_{DNS}\cdot\boldsymbol{q}_m^\star \mathrm{d}y$ of the DNS field with eigenfunctions $\boldsymbol{q}_m^\star$ of

the adjoint of $\mathscr{L}$, $\mathscr{L}^*(\boldsymbol{q}^*) = \omega \boldsymbol{q}^*$, which is defined by $\int_{-1}^{+1} \mathscr{L}(\boldsymbol{q})\cdot\boldsymbol{q}^* \mathrm{d}y \equiv \int_{-1}^{+1} \boldsymbol{q}\cdot\mathscr{L}^*(\boldsymbol{q}^*)\mathrm{d}y$. The adjoint operator is

$$\mathscr{L}^*(\boldsymbol{q}^*) = \begin{pmatrix} k_x \overline{u}\,\widehat{\rho}_* + k_x \overline{a}^2 \widehat{u}_*/\overline{\rho} + (\mathrm{i}/\overline{\rho})\mathrm{d}(\overline{a}^2\widehat{v}_*)/\mathrm{d}y + k_z \overline{a}^2 \widehat{w}_*/\overline{\rho} \\ k_x \overline{u}\,\widehat{u}_* + k_x \overline{\rho}\,\widehat{\rho}_* \\ k_x \overline{u}\,\widehat{v}_* + \mathrm{i}\overline{\rho}\,\mathrm{d}(\widehat{\rho}_*)/\mathrm{d}y - \mathrm{i}(\mathrm{d}\overline{u}/\mathrm{d}y)\widehat{u}_* \\ k_x \overline{u}\,\widehat{w}_* + k_z \overline{\rho}\,\widehat{\rho}_* \end{pmatrix}, \tag{A3}$$

where $\widehat{v}_* = 0$ at $y = \pm 1$.

When the base flow is uniform (no y variation), the eigenfunctions from (A2) are irrotational, and the eigenvalues ω from (A2) and (A3) give phase speeds $c_x = \mathrm{Re}(\omega)/k_x$ that satisfy

$$\overline{u} - c_x = \pm\, \overline{a}\,[(\ell\pi/2k_x)^2 + 1]^{1/2}, \tag{A4}$$

where ℓ is the wall-normal wavenumber (note that ℓ is equivalent to the number of times $\widehat{\rho}$ and $\widehat{u}$ change sign between $-1 \leqslant y \leqslant +1$). In §3.1 we use the Case A mean profiles shown in figure 7 as the base flow and numerically compute solutions to (A2) and (A3) using a non-uniform, staggered-grid finite difference scheme, which leads to 'acoustic' (isentropic) eigenfunctions that do not satisfy the above phase relation and, in fact, have non-zero vorticity near the walls. Near the channel centreline, however, the eigenfunctions have a more typical acoustic behaviour. That is, the ratio of the dilatation to the enstrophy is very large and for each integer ℓ (number of sign changes in $\widehat{\rho}$) there are two eigenmodes, with one propagating upstream, and the other downstream, relative to the centreline velocity. The dashed curve in figure 5 represents the density field after the isentropic modes $\boldsymbol{q}_\ell$ that are recognized as acoustic in the range $\ell = [0,1,2]$ have been projected and removed, for $k_x L_x/2\pi = [0,1,2]$ (using conjugate symmetry to account for $k_x < 0$) and $k_z L_z/2\pi = 0$. Only the eigenfunctions with (*a*) very large dilatation-to-enstrophy ratio near the centreline, and (*b*) no more than two modes at each ℓ – one with positive and one with negative relative phase speed – are chosen from the full inviscid isentropic function space to be included in the projection. These modes are practically indistinguishable from those found from a more general non-isentropic analysis (suggested to us by Professor S. K. Lele), which replaces (A1*c*) by $p' - \overline{T}\,\rho'/M^2 = \overline{p}\,s'$, where s' is the entropy fluctuation, and uses

$$\frac{\partial s'}{\partial t} + \overline{u}\frac{\partial s'}{\partial x} + v'\frac{\partial \overline{s}}{\partial y} = 0, \tag{A5}$$

and assumes $\mathrm{d}\overline{p}/\mathrm{d}y = 0$ to obtain a non-isentropic counterpart to (A2):

$$\mathscr{L}(\widetilde{\boldsymbol{q}}) = \begin{pmatrix} k_x \overline{u}\,\widehat{p} + k_x \gamma \overline{p}\,\widehat{u} - \mathrm{i}\gamma\overline{p}\,\mathrm{d}\widehat{v}/\mathrm{d}y + k_z \gamma \overline{p}\,\widehat{w} \\ k_x \overline{u}\,\widehat{u} - \mathrm{i}(\mathrm{d}\overline{u}/\mathrm{d}y)\widehat{v} + k_x \widehat{p}/\overline{\rho} \\ k_x \overline{u}\,\widehat{v} - \mathrm{i}\mathrm{d}\widehat{p}/\mathrm{d}y/\overline{\rho} \\ k_x \overline{u}\,\widehat{w} + k_z \widehat{p}/\overline{\rho} \end{pmatrix}, \tag{A6}$$

where $\widehat{v} = 0$ at $y = \pm 1$. (Note that the dependent variables are now $\widetilde{\boldsymbol{q}}_\ell(\boldsymbol{k}, y) = (\widehat{p}(\boldsymbol{k}, y),\ \widehat{u}(\boldsymbol{k}, y),\ \widehat{v}(\boldsymbol{k}, y),\ \widehat{w}(\boldsymbol{k}, y))^{\mathrm{T}}_\ell$.) Therefore, provided criteria (*a*) and (*b*) are used to determine which modes are included in the projection, the relevant eigenfunctions can be obtained without invoking the isentropic assumption at the beginning of the analysis.

REFERENCES

ANTONIA, R. A. & KIM, J. 1994 Low-Reynolds number effects on near-wall turbulence. *J. Fluid Mech.* **276**, 61–80.

BLAISDELL, G. A., MANSOUR, N. N. & REYNOLDS, W. C. 1993 Compressibility effects on the growth and structure of homogeneous turbulent shear flow. *J. Fluid Mech.* **256**, 443–485.

BRADSHAW, P. 1977 Compressible turbulent shear layers. *Ann. Rev. Fluid Mech.* **9**, 33–54.

BRADSHAW, P. & FERRISS, D. H. 1971 Calculation of boundary layer development using the energy equation: compressible flow on adiabatic walls. *J. Fluid Mech.* **46**, 83–110.

BROWN, G. L. & ROSHKO, A. 1974 On density effects and large structure in turbulent mixing layers. *J. Fluid Mech.* **64**, 775–816.

BUELL, J. C. 1991 Direct simulations of compressible wall-bounded turbulence. *CTR Annual Research Briefs – 1990, Stanford University/NASA Ames.*

CHILDS, R. E. & REISENTHEL, P. H. 1995 Simulation study of compressible turbulent boundary layers. *AIAA Paper* 95-0582.

COLEMAN, G. N. 1993 Direct simulation of isothermal-wall supersonic channel flow. *CTR Annual Research Briefs – 1993, Stanford University/NASA Ames.*

COLEMAN, G. N., BUELL, J. C., KIM, J. & MOSER, R. D. 1993 Direct simulation of compressible wall-bounded turbulence. *Ninth Symp. on Turbulent Shear Flows, Kyoto, Japan, August 16–18, 1993.*

DUCROS, F., COMPTE, P. & LESIEUR, M. 1993 Ropes and lambda vortices in direct and large-eddy simulations of a high-Mach number boundary layer over a flat plate. *Turbulent Shear Flows 9* (ed. F. Durst *et al.*). Springer.

FERNHOLZ, H. H. & FINLEY, P. J. 1977 A critical compilation of compressible turbulent boundary layer data. *AGARD-AG-223.*

FERNHOLZ, H. H. & FINLEY, P. J. 1980 A critical commentary on mean flow data for two-dimensional compressible turbulent boundary layers. *AGARD-AG-253.*

FERNHOLZ, H. H., SMITS, A. J., DUSSAUGE, J.-P. & FINLEY, P. J. 1989 A survey of measurements and measuring techniques in rapidly distorted compressible turbulent boundary layers. *AGARD-AG-315.*

FLETCHER, C. A. J. 1994 *Computational Galerkin Methods.* Springer.

GUO, Y. & ADAMS, N. A. 1994 *Proc. 5th Summer Prog., NASA/Stanford Center for Turbulence Research.*

GUO, Y., KLEISER, L. & ADAMS, N. A. 1994 A comparison study of an improved temporal DNS and spatial DNS of compressible boundary layer transition. *AIAA Paper* 94-2371.

HATAY, F. F. & BIRINGEN, S. 1995 Direct numerical simulation of low-Reynolds number supersonic turbulent boundary layers. *AIAA Paper* 95-0581.

HUANG, P. G., BRADSHAW, P. & COAKLEY, T. J. 1993 A skin friction and velocity profile family for compressible turbulent boundary layers. *AIAA J.* **31**, 1600–1604.

HUANG, P. G. & COLEMAN, G. N. 1994 On the Van Driest transformation and compressible wall-bounded flows. *AIAA J.* **32**, 2110–2113.

HUANG, P. G., COLEMAN, G. N. & BRADSHAW, P. 1995 Compressible turbulent channel flows: DNS results and modelling. *J. Fluid Mech.* **305**, 185–218.

KIM, J., MOIN, P. & MOSER, R. 1987 Turbulence statistics in fully developed channel flow at low Reynolds number. *J. Fluid Mech.* **177**, 133–166.

KOVÁSZNAY, L. S. G. 1953 Turbulence in supersonic flow. *J. Aeronaut. Sci.* **20**, 657–682.

LEE, M. J., KIM, J. & MOIN, P. 1990 Structure of turbulence at high shear rate. *J. Fluid Mech.* **216**, 561–583.

LELE, S. K. 1989 Direct numerical simulation of compressible free shear flows. *AIAA Paper* 89-0374.

LELE, S. K. 1994 Compressibility effects on turbulence. *Ann. Rev. Fluid Mech.* **26**, 211–254.

MORKOVIN, M. V. 1964 Effects of compressibility on turbulent flows. In *Mechanique de la Turbulence* (ed. A. Favre), pp. 367–380. Gordon & Breach.

PAPAMOSCHOU, D. & ROSHKO, A. 1986 Observations of supersonic free shear layers. *AIAA Paper* 86-0162.

PAPAMOSCHOU, D. & ROSHKO, A. 1988 The compressible turbulent shear layer: an experimental study. *J. Fluid Mech.* **197**, 453–477.

RAI, M. M., GATSKI, T. B. & ERLEBACHER, G. 1995 Direct simulation of spatially evolving compressible turbulent boundary layers. *AIAA Paper* 95-0583.

ROBINSON, S. K. 1991 Coherent motions in the turbulent boundary layer. *Ann. Rev. Fluid Mech.* **23**, 601–639.

SANDHAM, N. D. & REYNOLDS, W. C. 1991 Three dimensional simulations of large eddies in the compressible mixing layer. *J. Fluid Mech.* **224**, 133–158.

SETTLES, G. S. & DODSON, L. J. 1991 Hypersonic shock/boundary layer interaction database. *NASA Contractor Rep.* 177577.

SPALART, P. R. 1988 Direct simulation of a turbulent boundary layer up to $Re_\theta = 1410$. *J. Fluid Mech.* **187**, 61–98.

SPEZIALE, C. G. & SARKAR, S. 1991 Second-order closure models for supersonic turbulent flows. *AIAA Paper* 91-0212.

SPINA, E. F., SMITS, A. J. & ROBINSON, S. K. 1994 The physics of supersonic turbulent boundary layers. *Ann. Rev. Fluid Mech.* **26**, 287–319.

TEMPERTON, C. 1985 Implementation of a self-sorting in-place prime factor FFT algorithm. *J. Comput. Phys.* **58**, 283–299.

ZEMAN, O. 1990 Dilatation dissipation: The concept and application in modeling compressible mixing layers. *Phys. Fluids* A **2**, 178–188.